ACS NANO
Cite This: ACS Nano 2018, 12, 7220–7231
www.acsnano.org

ARTICLE

Cobalt Disulfide Nanoparticles Embedded in Porous Carbonaceous Micro-Polyhedrons Interlinked by Carbon Nanotubes for Superior Lithium and Sodium Storage

Yuan Ma,[†,‡] Yanjiao Ma,[†,‡] Dominic Bresser,[†,‡] Yuanchun Ji,[§] Dorin Geiger,[∥] Ute Kaiser,[∥] Carsten Streb,[†,§] Alberto Varzi,*[,†,‡] and Stefano Passerini*[,†,‡]

[†]Helmholtz Institute Ulm (HIU), Helmholtzstrasse 11, D-89081 Ulm, Germany
[‡]Karlsruhe Institute of Technology (KIT), P.O. Box 3640, D-76021 Karlsruhe, Germany
[§]Institute of Inorganic Chemistry I, Ulm University, Albert-Einstein-Allee 11, D-89081 Ulm, Germany
[∥]Central Facility for Electron Microscopy, Group of Electron Microscopy of Materials Science, Ulm University, Albert-Einstein-Allee 11, D-89081 Ulm, Germany

Supporting Information

ABSTRACT: Transition metal sulfides are appealing electrode materials for lithium and sodium batteries owing to their high theoretical capacity. However, they are commonly characterized by rather poor cycling stability and low rate capability. Herein, we investigate CoS_2, serving as a model compound. We synthesized a porous CoS_2/C micro-polyhedron composite entangled in a carbon-nanotube-based network (CoS_2-C/CNT), starting from zeolitic imidazolate frameworks-67 as a single precursor. Following an efficient two-step synthesis strategy, the obtained CoS_2 nanoparticles are uniformly embedded in porous carbonaceous micro-polyhedrons, interwoven with CNTs to ensure high electronic conductivity. The CoS_2-C/CNT nanocomposite provides excellent bifunctional energy storage performance, delivering 1030 mAh g^{-1} after 120 cycles and 403 mAh g^{-1} after 200 cycles (at 100 mA g^{-1}) as electrode for lithium-ion (LIBs) and sodium-ion batteries (SIBs), respectively. In addition to these high capacities, the electrodes show outstanding rate capability and excellent long-term cycling stability with a capacity retention of 80% after 500 cycles for LIBs and 90% after 200 cycles for SIBs. *In situ* X-ray diffraction reveals a significant contribution of the partially graphitized carbon to the lithium and at least in part also for the sodium storage and the report of a two-step conversion reaction mechanism of CoS_2, eventually forming metallic Co and Li_2S/Na_2S. Particularly the lithium storage capability at elevated (dis-)charge rates, however, appears to be substantially pseudocapacitive, thus benefiting from the highly porous nature of the nanocomposite.

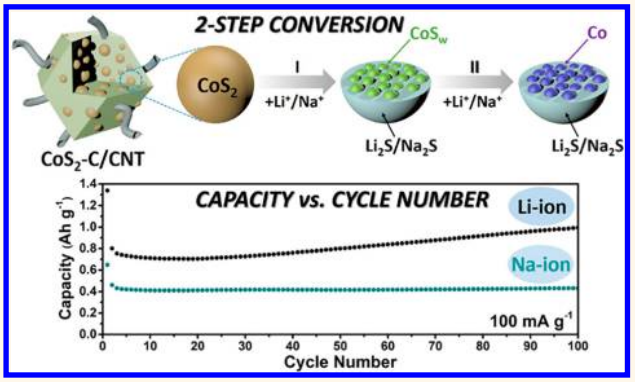

KEYWORDS: *lithium- and sodium-ion batteries, metal sulfide nanoparticles, porous carbonaceous frameworks, carbon nanotubes, in situ XRD/reaction mechanism*

To reduce the excessive consumption of fossil fuels and to foster the rapidly increasing use of electric vehicles (EVs), there is a tremendous push toward the development of high-energy and power rechargeable batteries, particularly, lithium-ion batteries (LIBs), as the state-of-the-art battery technology for portable and automotive applications.[1−3] In addition, due to potential cost advantages and greater natural abundance, sodium-ion batteries (SIBs) are increasingly investigated, especially for large-scale energy storage applications.[4] In this regard, the exploration of alternative electrode materials, providing high cycling stability and high specific capacities in combination with an advanced power density and safety, is a major challenge for lithium- and sodium-ion battery research.[1,4]

Received: April 27, 2018
Accepted: June 25, 2018
Published: June 25, 2018

DOI: 10.1021/acsnano.8b03188
ACS Nano 2018, 12, 7220–7231

Scheme 1. Schematic drawing of the formation process to obtain the CoS_2-C/CNTs nanocomposite.

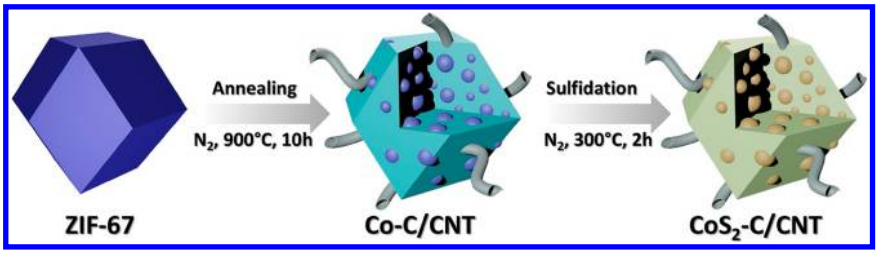

To address LIBs'/SIBs' issues, many alternative electrode materials have been developed during the past decade, such as transition metal oxides/sulfides/phosphides, even metal phosphonates.[5−8] Transition metal sulfides (TMSs, *e.g.*, FeS_2, CoS_2, MnS, ZnS, and MoS_2) are promising alternative active materials, as they provide improved safety and higher theoretical capacity, arising from the conversion reaction, which leads to the formation of metallic TM and Li/Na sulfides.[5] Compared to other conversion materials such as oxides, the metal−sulfur bonds are more easily broken during the conversion reaction with lithium or sodium, thus promising enhanced reaction kinetics.[9] Among the different TMSs, substantial research efforts have been devoted to cobalt disulfide (CoS_2) as an ideal model compound for both lithium and sodium storage, providing a large theoretical capacity (870 mAh g^{-1} for both LIBs and SIBs) and high conductivity.[10] Nevertheless, CoS_2-based anodes—just like other transition metal sulfides—suffer from serious drawbacks such as (i) severe volume variation upon repeated (de)lithiation or (de)sodiation, resulting in electrode pulverization and, thus, poor cycling stability, and (ii) rapid specific capacity fading due to polysulfide dissolution in the electrolyte.[10] In order to improve the electrochemical performance of metal sulfide-based electrodes, many strategies have been proposed. According to previous works, downsizing the metal sulfide particles to the nanoscale could significantly reduce the mechanical stress associated with the conversion reaction, thus relieving the pulverization issue.[10,11] Most importantly, employing a porous carbon matrix (*e.g.*, graphene or carbon nanotubes; CNTs) to host the TMS nanoparticles or embedding them in a carbon shell could further improve the electrochemical performance by increasing the electronic conductivity, capturing/adsorbing the polysulfide intermediates, and avoiding the agglomeration of the TMS nanoparticles.[6,7,10,12] In addition, the use of a carbonaceous structure can also lead to (i) reduced diffusion pathways for ions and (ii) improved flexibility to compensate the volume expansion, thus improving both cycling stability and reversibility of the conversion reaction.[6,7,9,10] According to these benefits, the fabrication of composite materials by embedding, for instance, nanoscale CoS_2 particles in a carbon matrix is an appealing approach to improve both LIB and SIB performance.

Metal organic frameworks (MOFs), a class of porous inorganic−organic hybrid materials, have been widely employed for many applications (*e.g.*, gas separation/storage, drug delivery, and catalysis) because of their high surface area, porous structure, and large pore volume.[13−15] Especially in energy storage, previously reported works have demonstrated that MOFs can act as template precursors for the synthesis of micro/nanostructured active materials, such as porous carbons with metal or metal oxide/sulfide composite materials.[14] Furthermore, through the optimization of annealing conditions, advanced micro/nanostructures could be obtained. Prime examples are MOF-based metal nanoparticles uniformly embedded in a porous carbon matrix linked by CNTs.[12,14] Therefore, it is a promising strategy to prepare a composite of nanostructured CoS_2 embedded in carbon by using a single Co-based MOF as precursor, *e.g.*, zeolitic imidazolate frameworks-67 (ZIF-67), which is rich in carbon and metallic cobalt and easily synthesized.[16] Wang *et al.* first developed a self-templated method (ZIF-67 as template) for the preparation of porous CoS_2/C micro-polyhedrons that delivered an initial reversible capacity of approximately 700 mAh g^{-1} and a capacity of 560 mAh g^{-1} (50th cycle) at a specific current of 100 mA g^{-1} in LIBs.[10] However, these electrodes showed a relatively low capacity and poor cycling stability (below 80% capacity retention after 50 cycles), possibly arising from the low conductivity of the carbon matrix. Using the same ZIF-67 as the parental compound, Lou and co-workers reported a hollow Co/C nanohybrid with CNTs by introducing reducing gas (H_2) during the annealing step.[12] The resulting CoS_2/C exhibits improved LIB performance due to the high graphitization degree. Li *et al.* also fabricated "dragon fruit"-like nanostructured CoS_2/C from ZIF-67, which could maintain a capacity of 510 mAh g^{-1} (~90% capacity retention) after 100 cycles as anode for SIBs.[17] Despite these continuous improvements, it is still a great challenge to fabricate advanced nanostructured CoS_2/C composites, especially including highly conductive CNT networks using a facile method, and simultaneously meeting both LIBs' and SIBs' demands.

In the present work, we report an efficient and high-yield two-step synthesis starting from a ZIF-67 precursor. The fabrication route leads to CoS_2-C/CNT composites where uniform CoS_2 nanoparticles are embedded in a porous carbonaceous micro-polyhedron framework that is interwoven by CNTs. Interestingly, the highly conductive CNT network is generated by direct annealing in a N_2 atmosphere without introducing any reducing gas and/or auxiliary agents.[12,18] We intensively investigated the physicochemical characteristics and the electrochemical performance of this composite. As a result of the combination of many favorable characteristics, including a pore structure and optimized graphitization degree of the incorporated carbon, the as-obtained CoS_2-C/CNT nanocomposite shows excellent bifunctional energy storage performance as anode material for LIBs and SIBs. Moreover, we demonstrate that the significant pseudocapacitive charge storage leads to an improved charge transfer rate during the (de)lithiation process, while the performance in SIBs is enhanced by substituting the commonly used carbonate-based electrolyte with an ether-based one (dimethoxyethane (DME)). Finally, the underlying reaction mechanism and the corresponding structural transitions upon (de)lithiation and (de)sodiation are studied *via in situ* X-ray diffraction (XRD), and a multistep conversion mechanism is proposed for both cationic charge carriers.

DOI: 10.1021/acsnano.8b03188
ACS Nano 2018, 12, 7220−7231

RESULTS AND DISCUSSION

Synthesis and Characterization of CoS_2-C/CNT. The two-step synthesis process for obtaining the CoS_2-C/CNT nanocomposite is illustrated in Scheme 1. As described in detail in the Methods section, the ZIF-67 precursor was synthesized by co-precipitation of 2-methylimidizole with divalent cobalt nitrate in methanol.

Scanning electron microscopy (SEM) images show the uniform rhombic dodecahedron morphology and the smooth particle surface of the precursor (see Figure 1a). The solid inner

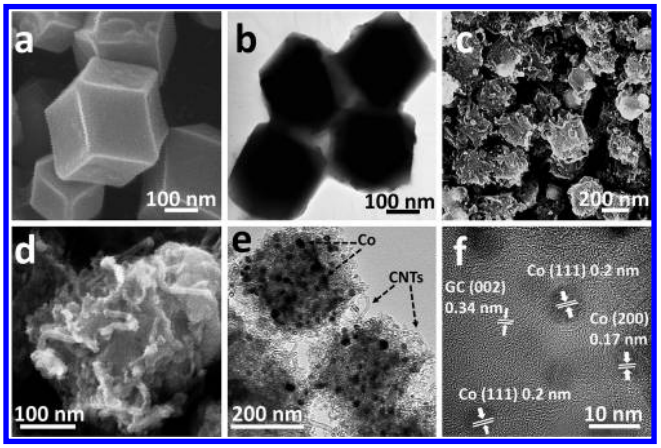

Figure 1. Morphological and structural features of the ZIF-67 precursor and the Co-C/CNT intermediate; SEM and (HR)TEM images of ZIF-67 (a, b) and Co-C/CNT (c–f); the lattice fringes highlighted in (f) are in good agreement with the JCPDS reference card no. 15-0806 for metallic cobalt and the characteristic (002) interlayer spacing for graphitic carbon.

structure of these micro-polyhedrons with an average size of about 300 nm is revealed by means of transmission electron microscopy (TEM, Figure 1b). In the first step of the synthesis, ZIF-67 is converted into a Co/C composite including also CNTs (Co-C/CNT). Accordingly, this step includes two subprocesses: (i) the generation and nucleation of uniform metallic Co nanoparticles and (ii) the formation of CNTs on the surface of the micro-polyhedrons and graphitized carbon (both carbon sources are derived from the organic ligands), catalyzed by the highly active metallic Co nanocatalyst and promoted by long-time calcination at relatively high temperature.[19,20] The powder XRD pattern in Figure S1 confirms that the intermediate is composed of metallic Co and graphitized carbon.

Further morphological and structural information are obtained from SEM and TEM analysis. The SEM images displayed in Figure 1c,d show that the Co-C/CNT composite retains the original size and micro-polyhedron shape of the ZIF-67 precursor, although a much rougher surface is obtained after annealing. Interestingly, the micro-polyhedron particles appear entangled in a network of CNTs with an outer diameter of *ca.* 15 nm. From the TEM micrograph (Figure 1e), the metallic Co nanoparticles are homogeneously dispersed within the micro-polyhedron carbon particles, which, in turn, are connected by the CNTs.[10,18] Meanwhile, a statistical TEM analysis of the particle size, presented in Figure S2a and b, revealed that the metallic Co nanoparticles have a size of *ca.* 20–26 nm, indicating a slight particle agglomeration, probably due to the high annealing temperature of the pure Co-based ZIFs.[10,18] However, the dark metallic Co nanoparticles are uniformly coated by a thin graphitized carbon layer (with the *d*-spacing of 0.34 nm corresponding to the C(002) plane, as shown in Figure 1f). The encapsulated dark nanoparticles with interlayer distances of ~0.2 and ~0.17 nm could be attributed to the (111) and (200) lattice planes of cubic metallic Co (JCPDS card no. 15-0806), respectively.

Next, in order to obtain electrochemically active CoS_2, the Co-C/CNT composite was oxidized with elemental sulfur under mild conditions.[12] The powder XRD pattern shown in Figure 2

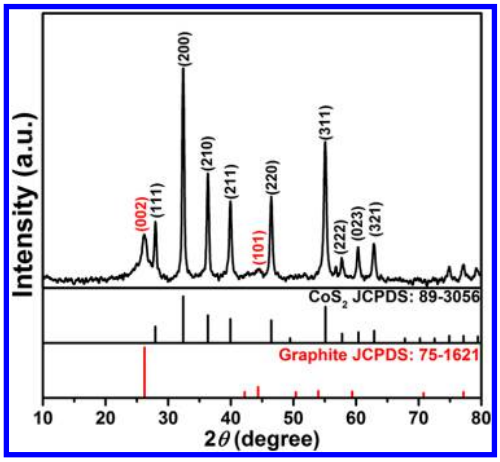

Figure 2. Powder XRD pattern of CoS_2-C/CNT. The references for CoS_2 (JCPDS card no. 89-3056) and graphite (JCPDS card no. 75-1621) are shown at the bottom.

is consistent with cubic CoS_2 (JCPDS card no. 89-3056) and graphitic carbon (JCPDS card no. 75-1621). Accordingly, the final product is denoted as CoS_2-C/CNT. We may note that the sample contains also some elemental sulfur according to the X-ray photoelectron spectroscopy (XPS) analysis (Figure S3), at least at the sample surface, which did not react with the contained metallic cobalt. To further analyze the nanocomposite, we employed SEM and TEM (Figure 3). According to Figure 3a, the CoS_2-C/CNT particles have a rather uniform micro-polyhedron shape, indicating that the original shape of the parent compounds (*i.e.*, the initial ZIF-67 precursor and the Co-C/CNT intermediate) is retained. The SEM images collected at higher magnification (Figure 3b,c) display a relatively rough surface for the quasi-polyhedron-shaped particles intertwined *via* the CNTs. The TEM micrographs (Figure 3d–f) reveal that the metal sulfide particles (dark dots) are uniformly embedded in the carbonaceous micro-polyhedron particles. Also, upon conversion of metallic Co to CoS_2, no evident change in size of the nanoparticles can be observed (see Figure S2c,d). Furthermore, similarly to the morphology observed for Co-C/CNT (Figure 3f,g) also for CoS_2-C/CNT the CNTs serve as a linkage between the carbonaceous micro-polyhedron particles, and the CNTs retain an average outer diameter of *ca.* 15 nm after sulfidation. The high-resolution transmission electron microscopy (HRTEM) micrographs, displayed in Figure 3h,i, reveal the lattice fringes of crystalline CoS_2 with a *d*-spacing of 0.25 nm for the (210) lattice plane. Moreover, the walls of the bamboo-like CNTs, with a thickness of around 3.5 nm (inner diameter of *ca.* 10 nm), reveal multiwall features and several crystalline defects between the cracked lattice fringes.[21] From Figure 3i it can be seen that the carbon layer, composed of graphitic and amorphous sections, is wrapped around the CoS_2 nanoparticle.[21,22] Overall, the (HR)TEM analysis reveals that the CoS_2 particles are mostly wrapped or coated with a carbon layer

DOI: 10.1021/acsnano.8b03188
ACS Nano 2018, 12, 7220–7231

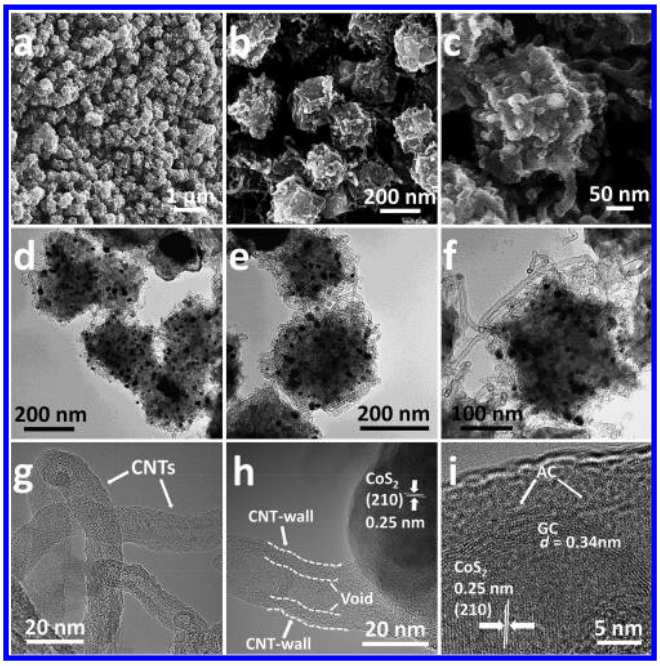

Figure 3. Morphological and structural features of CoS_2-C/CNT: (a–c) SEM images and (d–f) TEM micrographs at different magnifications; (g–i) HRTEM micrographs (AC = amorphous carbon and GC = graphitized carbon).

and remain inside the micro-polyhedrons. The energy-dispersive X-ray spectroscopy (EDX) mapping recorded in Figure S4 further confirms the uniform distribution of Co, S, and C within the CoS_2-C/CNT nanocomposite.

Thermogravimetric analysis (TGA) was performed to determine the CoS_2 content in the as-prepared CoS_2-C/CNT composite. As shown in Figure S5, 30 wt % of solid residue was obtained after conducting TGA in air. Considering the formation of Co_3O_4, we can estimate the amount of CoS_2 in CoS_2-C/CNT to around 46 wt %, which is in good agreement with the elemental analysis performed by inductively coupled plasma optical emission spectroscopy (ICP-OES) and EDX (see Table S1).[12,20] The Raman spectrum (Figure S6) reveals four distinct bands: the peak at 389 cm^{-1} can be assigned to CoS_2, while the 2D-peak at higher wavenumbers (2659 cm^{-1}) as well as the D- and G-bands, respectively at 1333 and 1582 cm^{-1}, are typical of partially graphitic carbon.[23,24] Interestingly, the intensity of the D-peak is slightly lower than the G-peak, suggesting, in combination with the presence of the 2D band, a relatively high content of sp^2-hybridized carbon.[25,26] The determination of the electronic conductivity reveals that the presence of such well-graphitized carbon leads to a relatively high conductivity of 1.2 S cm^{-1} (see Table S2, including also a comparison with comparable composites), which is presumably beneficial for its performance as lithium- and sodium-ion electrodes.

In addition, the surface area and pore size distribution of CoS_2-C/CNT were quantified by N_2 sorption (Figure S7). CoS_2-C/CNT features a moderate specific Brunauer–Emmett–Teller (BET) surface area of 139.7 m^2 g^{-1} (see Figure S7a). The pore size distribution, calculated according to the Barrett–Joyner–Halenda (BJH) method (see Figure S7b), reveals the hierarchical micro/mesoporosity of CoS_2-C/CNT, with pore size centered at ~1.9 and ~13 nm.[27,28] The smaller pores presumably result from the presence of the amorphous carbon micro-polyhedrons, while the relatively larger pores are, in fact, in good agreement with the inner diameter of the CNTs and/or may result from the connection of adjacent small pores.[29]

Characterization as Lithium-Ion Active Material and *in Situ* XRD Analysis. The electrochemical performance of the CoS_2-C/CNT composite was first investigated as active material for lithium-based batteries. The results for the initial cyclic voltammetry (CV) are shown in Figure 4a. In the initial cathodic

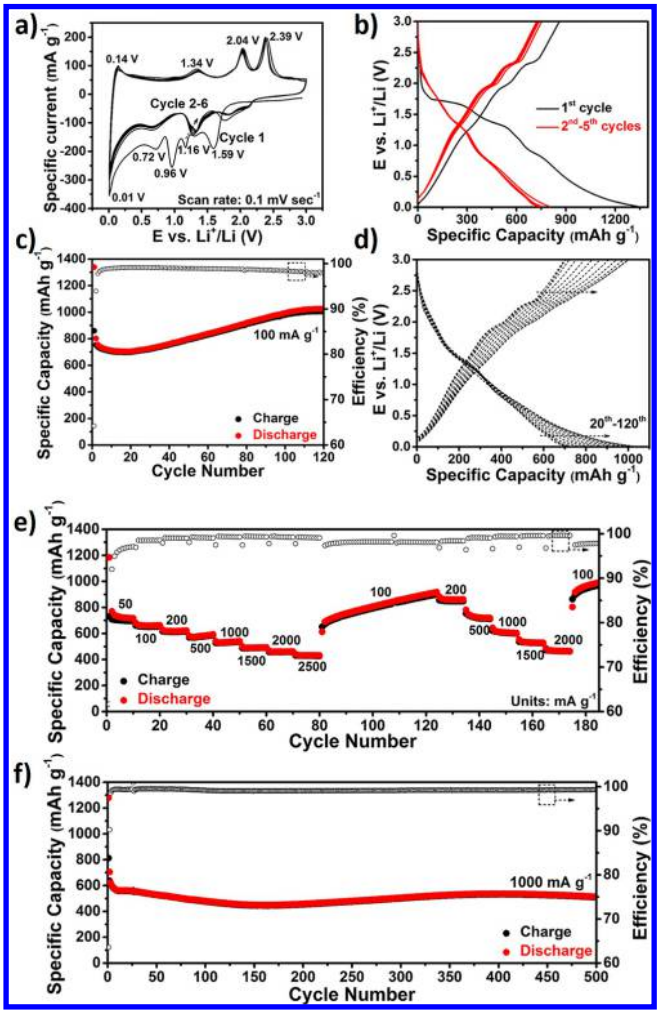

Figure 4. Electrochemical performance of CoS_2-C/CNT-based electrodes in lithium half-cell configuration. (a) Cyclic voltammetry conducted in a potential range of 0.01–3.0 V for six cyclic sweeps (scan rate: 0.1 mV s^{-1}). (b) (Dis-)charge profiles for the first five galvanostatic cycles at a specific current of 100 mA g^{-1}. (c) "Capacity *vs* cycle number" plot for 120 galvanostatic cycles, applying a constant specific current of 100 mA g^{-1}. (d) Selected (dis-)charge profiles for the 20th, 30th, 40th, 50th, 60th, 70th, 80th, 90th, 100th, 110th, and 120th cycle. (e) Rate capability test, applying various specific currents ranging from 50 to 2500 mA g^{-1} for 185 cycles in total. (f) "Capacity *vs* cycle number" plot for electrodes subjected to a specific current of 1000 mA g^{-1} for 500 cycles.

scan, the three peaks at *ca.* 1.59, 1.16, and 0.96 V can be attributed to the reduction of CoS_2 to Co^0 and Li_2S.[30] Furthermore, a small peak centered at around 0.72 V is observed, and the corresponding oxidation peak appears at 1.34 V in the initial anodic scan. Kong *et al.* proposed that the peak at 0.72 V can be assigned to the formation of the solid electrolyte

DOI: 10.1021/acsnano.8b03188
ACS Nano 2018, 12, 7220–7231

interphase (SEI), while its related anodic peak (1.34 V) corresponds to the partial decomposition of the SEI layer.[31] However, the origin of this peak couple will be discussed later based on *in situ* powder XRD analysis. The peak below 0.4 V may be ascribed to the lithium-ion intercalation/insertion into the carbon (including the conductive additive), which is further confirmed by the minor peak at 0.14 V for the subsequent anodic sweep.[32,33] The two intense features at 2.04 and 2.39 V can be assigned to the resulfidation of Co^0 to form the metal sulfide. For the subsequent cycles, besides a slight upshift of the reduction peaks to about 1.75 and 1.32 V, the CVs essentially overlap, confirming the promising reversibility of the CoS_2-C/CNT anode materials during repeated (de)lithiation.[32]

Figure 4b shows the initial five (dis-)charge profiles, for electrodes subjected to galvanostatic cycling. Several short plateaus are detected, which are in good agreement with the redox processes observed in the CV experiment. In the first cycle, the CoS_2-C/CNT-based electrode provides a large discharge and charge specific capacity of 1339 and 860 mAh g^{-1}, respectively. The reversible capacity is slightly lower than the theoretical value of 870 mAh g^{-1}, not least due to the carbon component[34] (representing slightly more than half of the total active material), which is included for the calculation of the capacity obtained, but contributes only about 500 mAh g^{-1} reversible capacity in the first cycle (Figure S8). The rather low Coulombic efficiency of 64.2% is attributed to (i) the formation of the SEI layer and (ii) the partial irreversibility of the conversion (CoS_2) and/or insertion (C and CNT) processes (see also Figure S8). Interestingly, the Coulombic efficiency rapidly increases to 94% in the second cycle and 99% in the fifth cycle, confirming that these irreversible processes are limited to the initial (de)lithiation cycle. Figure 4b also reveals the overlapping potential profiles of the second to fifth cycles, corresponding to the CV measurement, and the CoS_2-C/CNT electrode has excellent reversibility during repeated (de)-lithiation. The extended galvanostatic (dis-)charge testing (Figure 4c) revealed an excellent cycling stability for CoS_2-C/CNT. Initially, the specific capacity slightly decreased to around 700 mAh g^{-1} between the fifth and the 20th cycle prior to a continuous increase up to the 120th cycle, after which it eventually stabilizes at *ca.* 1030 mAh g^{-1}.

Considering the evolution of the corresponding potential profiles (Figure 4d) reveals that the capacity increase mainly originates from an increase in discharge capacity at rather low (*i.e.*, <0.8 V) and in charge capacity at rather high (>2.3 V) potentials. We assign this capacity growth in large part to the "quasi-reversible" SEI formation, reported earlier for other conversion materials.[22,25,35,36] Nevertheless, the Coulombic efficiency of this hybrid anode still is higher than 99% between the 10th and 60th cycle, before slightly declining to 98% toward the 120th cycle. The *ex situ* SEM analysis of cycled electrodes based on CoS_2-C/CNT after 60 and 120 cycles (Figure S9a and b, respectively) shows that the initial micro-polyhedron particle shape is lost upon cycling, presumably due to the volume changes.[22,37] Moreover, Figure S9b nicely reveals the formation of a thick SEI layer after 120 cycles, far thicker than the SEI layer formed after 60 cycles (Figure S9a), which is in agreement with our explanation concerning the origin of the increase in capacity. Both these phenomena of *ex situ* SEM analysis can account for the decreased Coulombic efficiency observed between the 60th and 120th cycle.[22,37]

In addition to characteristics such as specific capacity and cycling stability, the rate capability of potential battery materials is of great importance. Accordingly, we subjected CoS_2-C/CNT-based electrodes to varying specific currents, ranging from 50 to 2500 mA g^{-1}. As depicted in Figure 4e, the electrodes present a stable performance at all C rates investigated. For specific currents of 50, 100, 200, 500, 1000, 1500, and 2000 mA g^{-1}, an average specific capacity of around 730, 664, 620, 582, 535, 492, and 461 mAh g^{-1} is obtained, respectively. For the highest applied current of 2500 mA g^{-1}, the electrode can still deliver 433 mAh g^{-1}. When the current is subsequently lowered back to 100 mA g^{-1}, a specific capacity of 690 mAh g^{-1} (82nd cycle) is observed, indicating a good capacity retention. Afterward a steady capacity increase is observed once more, reaching 917 mAh g^{-1} at the 124th cycle. Accordingly, the capacity values for the second C rate test slightly increased to *ca.* 864, 732, 612, 533, and 470 mAh g^{-1} at 200, 500, 1000, 1500, and 2000 mA g^{-1}, respectively. After decreasing the current once again from 2000 to 100 mA g^{-1}, the specific capacity slightly increased further up to 992 mAh g^{-1} for the 185th cycle, revealing that the CoS_2-C/CNT composite electrode can maintain excellent stability and reversibility, even after undergoing two intervals of elevated C rate cycling. Additionally, the long-term cycling stability under a high current density of 1000 mA g^{-1} was also evaluated (see Figure 4f). It is worth noting that CoS_2-C/CNT consistently delivers more than ~460 mAh g^{-1} for 500 cycles and up 500 mAh g^{-1} for the last 220 cycles (280–500th) with Coulombic efficiency approaching 100% from the fifth to the 500th cycle. Overall, after 500 cycles a capacity retention of about 80% can be observed (with respect to the second cycle). A comparison of the Li-ion storage performance with previous studies on CoS_2 or CoS_2-based composite is provided in Tables S3 and S4, indicating the superior electrochemical performance of CoS_2-C/CNT in terms of cycling stability and rate capability with regard to the great majority of previous works.

In order to better understand the excellent rate performance, we performed a kinetic study by means of cyclic voltammetry (Figure 5). Generally, the total Li-ion charge storage includes two contributions: diffusion- (intercalation/conversion/alloying process) and (pseudo)capacitive-controlled charge storage.[38] The pseudocapacitive contribution can be qualitatively demonstrated on the basis of CV experiments when applying varying scan rates.[38−40]

Figure 5a and Figure S10 show the CV data for the different sweep rates and show that the general shape is retained between 0.1 and 1.0 mV s^{-1} (Figure 5a), indicating minor polarization at these rates. According to previous studies by Dunn and coworkers,[39,40] one can obtain the degree of the pseudocapacitive contribution by determining the relationship between the measured peak current (i) and the scan rate (v) according to the following formulas:

$$i = av^b \tag{1}$$

$$\log i = b \log v + \log a \tag{2}$$

where a is a constant. b is determined by the slope of log i *vs* log v (see Figure 5b and eq 2). A b value of 0.5 or 1.0 indicates an ideal diffusion-dominated process or a surface-determined, capacitive-controlled behavior, respectively.[38−40] The calculated b values for CoS_2-C/CNT are displayed in Figure 5b. Values of 0.85 and 0.73 are found for the cathodic and anodic current peaks, respectively, suggesting that both diffusion-limited charge storage and capacitive behavior contribute to the observed capacities. Furthermore, by dividing the current response i at a

DOI: 10.1021/acsnano.8b03188
ACS Nano 2018, 12, 7220−7231

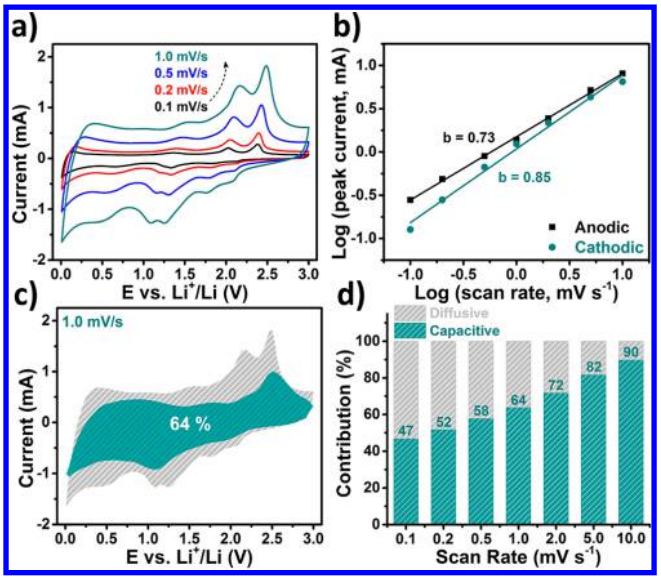

Figure 5. Kinetic analysis of the lithium storage contributions for CoS_2-C/CNT electrodes. (a) CV curves at different sweep rates. (b) Calculation of the *b* value (see eqs 1 and 2)) by plotting the logarithmic peak current (log *i*) *vs* the logarithm of the applied scan rate (log *v*). (c) Illustration of the capacitive- (cyan area) and diffusion-controlled (gray area) contributions to the overall charge storage, exemplarily depicted for a scan rate of 1.0 mV s^{-1}. (d) Percentage of the pseudocapacitive contribution to the overall recorded capacity as a function of the applied scan rate, ranging from 0.1 to 10.0 mV s^{-1} (see Figure S10 for the corresponding CV data at scan rates of >1.0 mV s^{-1}).

fixed potential into capacitive effect (k_1v) and diffusion-controlled process ($k_2v^{1/2}$), the more precise percentage of capacitive contributions can be obtained using eq 3:

$$i(V) = k_1v + k_2v^{1/2} \quad (3)$$

where both k_1 and k_2 are constants for a given voltage. The corresponding k_1 value at a particular potential can be determined as the slope of the curve resulting from the plot of $i(V)/v^{1/2}$ *vs* $v^{1/2}$, while the intercept corresponds to the k_2 value. The obtained results are presented in Figure 5c, showing that *ca.* 64% of the total capacity (cyan area) is derived from pseudocapacitive processes for a scan rate of 1.0 mV s^{-1}. As expected, when increasing the scan rate, the capacitive contribution continuously increases, reaching values as high as 90% at 10.0 mV s^{-1} (Figure 5d). Such high pseudocapacitive contribution presumably originates from the hierarchical porous structure and the large surface area of the carbonaceous micropolyhedrons entangled by CNTs, thus largely contributing to the excellent rate capability.[38−41]

To further investigate the electrochemical reaction mechanism of CoS_2-C/CNT, *in situ* XRD analysis was performed during the first lithiation (from open-circuit voltage (OCV) to 0.01 V) and delithiation (0.01 to 3.0 V). All collected XRD patterns (73 scans) are reported in Figure 6a (left panel), including the corresponding potential profile of the first cycle (right panel). Based on the different electrochemical behavior, the voltage profile can be divided into six regions, which are indicated in the waterfall XRD panel by olive patterns. In region 1 (OCV to 1.45 V, lithiation), the potential profile presents a distinct plateau (corresponding to the first cathodic peak at around 1.59 V in the CV curves, see Figure 4a). The corresponding XRD patterns (scans 1 to 13) reveal a sharp intensity decline for the CoS_2 reflections, until their complete disappearance at scans 10−12 (see also Figure 6b, upper left, *i.e.*, region 1). At the same time, a series of new reflections (27° (present as a shoulder), 31.2°, and 44.7°) appear, indicating the formation of Li_2S (JCPDS card no. 01-089-1930). Furthermore, a new signal at *ca.* 30° evolves gradually, matching with the

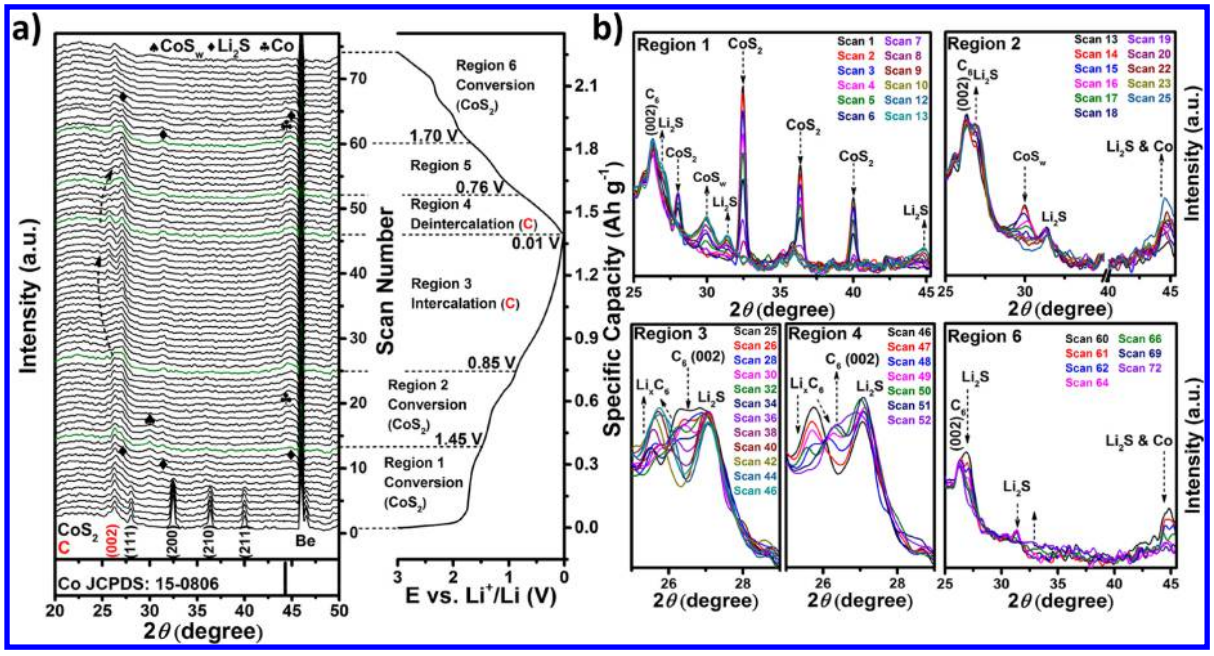

Figure 6. *In situ* XRD analysis of galvanostatically (dis-)charged electrodes comprising CoS_2-C/CNT as active material, cycled *vs* lithium metal. (a) Waterfall plot of the consecutively recorded XRD patterns (scans 1 to 73; in the bottom the JCPDS reference (card no. 15-0806) for metallic cobalt is given) and the corresponding (dis-)charge profile. (b) Selected regions of the waterfall plot according to the different occurring electrochemical reactions and distinguished features of the (dis-)charge profile.

DOI: 10.1021/acsnano.8b03188
ACS Nano 2018, 12, 7220−7231

reference for Co_9S_8 (JCPDS card no. 86-2273). Therefore, in contrast to previous reports,[22,25,42] our XRD results suggest that in the initial lithiation stage CoS_2 does not undergo Li insertion, but it is rather converted to Li_2S and sulfur-poor CoS_w.

Upon further lithiation to 0.85 V (region 2) the galvanostatic voltage profile exhibits two small plateaus at about 1.34 and 0.92 V, corresponding to the two cathodic peaks at around 1.16 and 0.96 V in the CV curves (see Figure 4a), respectively. A careful study of the related XRD patterns (scan 13 to 25 in Figure 6b, upper right, *i.e.*, region 2) reveals a continuous decrease in intensity of the sulfur-poor intermediate CoS_w phase, which fully vanishes between scan 20 and 22, accompanied by a gradual intensity increase for the reflections related to Li_2S. Simultaneously, an increase of the reflection at around 44−45° is detected, indicating an increasing presence of metallic Co (JCPDS card no. 15-0806). These results indicate that the conversion of CoS_2 to metallic Co and Li_2S is completed at 0.85 V. In sum, the initial reduction of CoS_2 undergoes successive two-step phase transformation, starting from $CoS_2 \rightarrow CoS_w \rightarrow Co^0$, accompanied by the concurrent formation of Li_2S.

In the last region of the lithiation profile (region 3, scans 25 to 46) from 0.85 to 0.01 V, two different regimes characterized by different slopes (the first in the range 0.85−0.51 V and the second between 0.51 and 0.01 V) are observed. No obvious change is observed anymore for the consecutive XRD pattern from scan 25 (*ca.* 0.85 V) to 29 (*ca.* 0.58 V, to be discussed later in more detail). Between scans 29 and 46, an obvious slope can be observed in the galvanostatic voltage profile, corresponding to the last cathodic peak at 0.01 V in the CV curves (see Figure 4a). After scan 29 (Figure 6b, bottom left), the intensity of the graphite (002) reflection at 26.4° slightly shifts to lower 2θ values and gradually decreases, whereas a new reflection appears at slightly lower angles (*ca.* 25.7°). This latter reflection continuously increases until the cell is fully discharged at 0.01 V (scan 46), indicating the intercalation of lithium into graphitized carbon to form Li_xC_6.[33]

During the following charge, in region 4 (from 0.01 to 0.76 V, *i.e.*, the anodic peak at 0.14 V in CV), the XRD patterns (scans 46 to 52) reveal the reversed behavior as for region 3; that is, the carbon (002) reflection reappears, evidencing the reversibility of the lithium intercalation process. Nonetheless, we may note also that the initial intensity is not fully recovered, suggesting that a certain extent of disorder is introduced in the carbon lattice.[43]

When the electrode is polarized further to 1.70 V (region 5, scans 52−60), a small plateau is observed at *ca.* 1.35 V for the potential profile, corresponding to the CV peak at 1.34 V. However, we do not observe any appreciable change for the XRD patterns in this region, while similar phenomena can also be found in region 3 from scan 25 to scan 29 (corresponding to the cathodic peak at 0.72 V recorded in CV). According to previous literature, there are two possible explanations for small plateaus in the (dis-)charge profiles and peak couples in the CV: (i) the SEI formation and partial decomposition, as claimed by Kong *et al.* and Zhang *et al.*[11,31] Nevertheless, the CV response indicates very high reversibility, which is somehow contradictory to common observations concerning the "quasi-reversible" SEI formation. (ii) Another explanation is the presence of a small fraction of electrochemically active, but (quasi-)amorphous species in the sample, *e.g.*, cobalt nitride. This assumption would be supported by the comparable CV data recorded in Wang's report,[10] following a similar synthesis method (*i.e.*, including nitrogen in the organic ligand), while this redox peak couple is absent for CoS_2 in rGO/MWCNTs.[44]

For the subsequent charge up to the cutoff potential of 3.0 V, *i.e.*, region 6 (1.70 to 3.0 V, scans 60 to 73, corresponding to the CV peaks at 2.04 and 2.39 V), a new, rather broad signal appears in the range from 31° to 36°, coupled with the rapid intensity decrease of the reflections related to Li_2S and metallic Co, eventually resulting in their complete disappearance at scans 70−72. According to previous studies,[22,25] this new signal may be attributed to the resulfidation of metallic Co to form CoS_2 and/or a mixture of CoS_2 and CoS_w.

In conclusion, based on the above-discussed results, we can propose the electrochemical reaction mechanism for the CoS_2-C/CNT anode upon the initial (de)lithiation process to proceed, including a two-step conversion reaction mechanism between CoS_2 and lithium ion, and the intercalation process between graphitized carbon/CNT and Li ion, as follows:

Region 1 (OCV−1.45 V, conversion)

$$CoS_2 + 2Li^+ + 2e^- \rightarrow CoS_w + Li_2S \text{ (not balanced)}$$

Region 2 (1.45−0.85 V, conversion)

$$CoS_w + 2wLi^+ + 2we^- \rightarrow Co^0 + wLi_2S$$

Region 3 (0.85−0.01 V, intercalation)

$$C_6 + x\,Li^+ + xe^- \rightarrow Li_xC_6$$

Region 4 (0.01−0.76 V, deintercalation)

$$Li_xC_6 \rightarrow C_6 + xLi^+ + xe^-$$

Region 6 (1.70−3.00 V, conversion)

$$Co^0 + 2Li_2S \rightarrow CoS_2 + 4Li^+ + 4e^-$$

and/or

$$2Co^0 + (2 + w)Li_2S \rightarrow CoS_2 + CoS_w + (4 + 2w)Li^+ + (4 + 2w)e^-$$

Characterization as Sodium-Ion Active Material and *in Situ* XRD Analysis. The CoS_2-C/CNT micro-polyhedron nanocomposite was also investigated as active material for Na-ion batteries. The electrochemical response when performing cyclic voltammetry is reported in Figure 7a. In the initial cathodic sweep, the first two peaks (at 1.15 and 0.73 V) are assigned to the multistep conversion reaction of CoS_2 to form metallic Co and Na_2S[45] and a small contribution from solvent co-intercalation and capacitive process in the graphitized carbon.[46,47] Additionally, the SEI layer is formed at 0.73 V.[11] Afterward, a sharp peak is observed at *ca.* 0.6 V, which mainly is attributed to the cointercalation of Na^+-solvent complexes into the graphitized carbon.[47] The relatively small peak below 0.15 V is assigned to the reversible Na storage in the conductive carbon, which appears highly reversible with respect to the small anodic peak at slightly higher potentials.[48] The following two, rather sharp peaks at 1.76 and 1.95 V in the first anodic scan are assigned to the decomposition of Na_2S, forming a metal sulfide.

The second cyclic sweep shows a shift of the cathodic peaks from 1.15, 0.73, and 0.6 V to 1.46, 0.9, and 0.57 V, respectively, indicating a significant structural reorganization after the initial sodiation. Also, the anodic peak at 1.95 V (in the first scan) splits into two peaks at 1.94 and 2.02 V, suggesting that also the desodiation process undergoes some changes after the first cyclic sweep. However, apart from a slight shift of the reduction peak recorded at 0.9 V in the second cycle to around 0.79 V upon continuous (de)sodiation, the voltammograms largely overlap

DOI: 10.1021/acsnano.8b03188
ACS Nano 2018, 12, 7220−7231

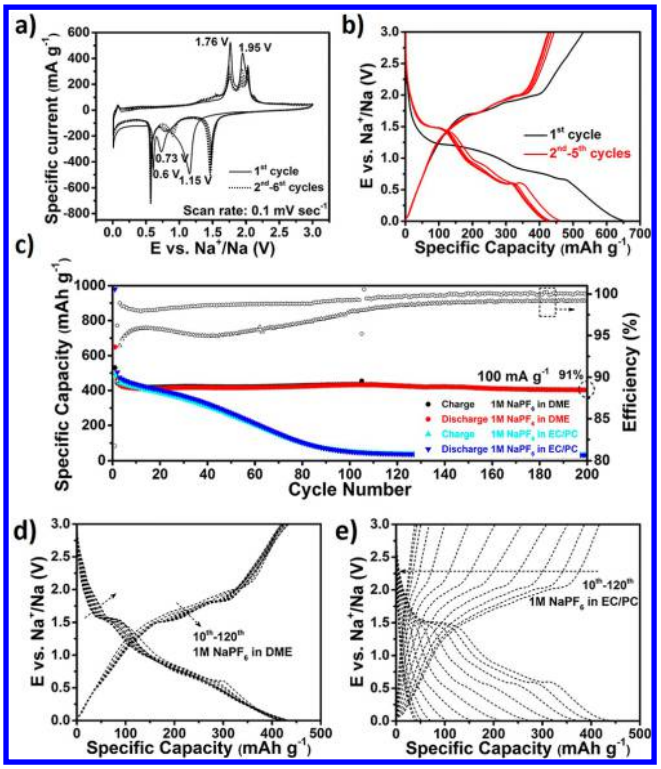

Figure 7. Electrochemical performance of CoS_2-C/CNT-based electrodes *vs* sodium metal. (a) Cyclic voltammetry carried out in a potential range from 0.01 to 3.0 V for six consecutive cycles (scan rate 0.1 mV s^{-1}) in 1 M $NaPF_6$−DME. (b) (Dis-)charge profiles of the first five cycles when applying a constant specific current of 100 mA g^{-1} in 1 M $NaPF_6$−DME. (c) "Capacity *vs* cycle number" plot for 200 cycles, applying a constant specific current of 100 mA g^{-1} in 1 M $NaPF_6$−DME (red and black) and, for comparison, in 1 M $NaPF_6$−EC/PC (dark and light blue); ○ and Δ are the Coulombic efficiency values for the cells cycled using 1 M $NaPF_6$−DME and 1 M $NaPF_6$−EC/PC, respectively. (d, e) Corresponding (dis-)charge profiles for selected cycles (10th, 20th, 30th, 40th, 50th, 60th, 70th, 80th, 90th, 100th, 110th, 120th) in (d) 1 M $NaPF_6$−DME and (e) 1 M $NaPF_6$−EC/PC.

from the fourth scan onward, confirming the reversible uptake and release of sodium after an initial "activation".[9]

The first five (dis-)charge profiles of galvanostatically cycled CoS_2-C/CNT-based electrodes *vs* sodium metal at 100 mA g^{-1} are displayed in Figure 7b and are in good agreement with the CV data. The initial discharge and charge capacities are 650 mAh g^{-1} and 530 mAh g^{-1}, respectively, which corresponds to a high first-cycle Coulombic efficiency of almost 82% in ether-based electrolyte ($NaPF_6$−DME). The larger discharge capacity originates from irreversible sodiation processes and, particularly, electrolyte decomposition and SEI layer formation. For the following cycles (3rd to 5th), a specific capacity of about 430 mAh g^{-1} is observed and the (dis-)charge profiles nicely overlap—just like for the CV experiment—confirming the high reversibility of the (de)sodiation process.

The long-term cycling performance at a current density of 100 mA g^{-1} is shown in Figure 7c. The reversible Na storage capacity of CoS_2-C/CNT in ether-based electrolyte remains excellent over 200 cycles, with 435 mAh g^{-1} at the 100th cycle and 402 mAh g^{-1} after 200 cycles, respectively accounting for ∼98% and ∼91% capacity retention with respect to the second cycle capacity (443 mAh g^{-1}). In the *ex situ* post mortem SEM and TEM images collected after 200 cycles (see Figure S11), although the original micro-polyhedron morphology is clearly lost, the CoS_2 nanoparticles still appear uniformly dispersed, confirming that the carbonaceous framework acts as a buffer, limiting volume variation, breakage, and agglomeration of the nanoparticles.[10] Contrarily, if cycled in carbonate-based electrolyte, the reversible capacity of the CoS_2-C/CNT electrode rapidly fades to ∼50 mAh g^{-1} within the first 100 cycles, indicating just 11.2% capacity retained from the second cycle (see Figure 7c). The poor cyclability is associated with a rather low Coulombic efficiency (∼96% at the 70th cycle) compared to the high reversibility observed in DME (CE gradually increasing to 99% after 70 cycles, finally stabilizing at 99.9% in the 135−200th cycle range). Such poor cycling stability comes along with a relatively low Coulombic efficiency, suggesting that the interfacial stability is of utmost importance for the reversibility of the electrochemical charge storage processes. The comparison of the corresponding (dis-)charge profiles in Figure 7d (1 M $NaPF_6$ in DME) and Figure 7e (1 M $NaPF_6$ in a mixture of ethylene carbonate/propylene carbonate (EC/PC; 1:1 by weight)) reveals well-overlapping potential profiles in the case of the ether-based electrolyte and rapid fading, accompanied by a substantially increasing polarization in the case of the carbonate-based one.

Figure 8 presents the rate capability of CoS_2-C/CNT-based electrodes in 1 M $NaPF_6$−DME (Figure 8a and c) and 1M

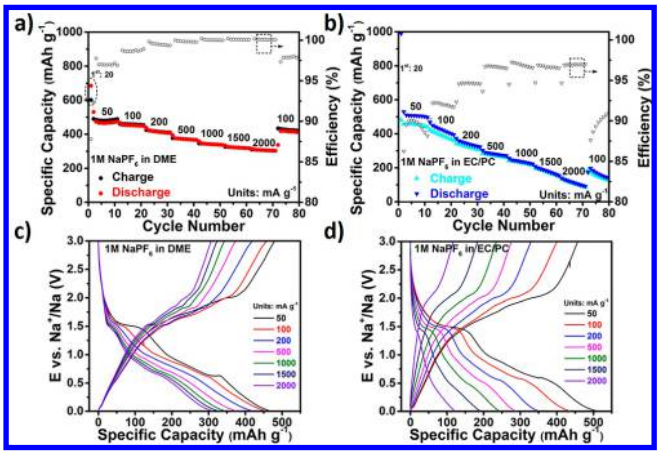

Figure 8. Rate capability of CoS_2-C/CNT anodes in sodium half-cells employing (a) 1 M $NaPF_6$−DME and (b) 1 M $NaPF_6$−EC/PC as electrolyte at different specific currents, ranging from 20 to 2000 mA g^{-1}, and the corresponding (dis-)charge profiles for cells incorporating (c) 1 M $NaPF_6$−DME and (d) 1 M $NaPF_6$−EC/PC for selected cycles (*i.e.*, the 5th, 15th, 25th, 35th, 45th, 55th, and 65th).

$NaPF_6$−EC/PC (Figure 8b and d) at progressively increasing currents, ranging from 50 to 2000 mA g^{-1}. Using the DME-based electrolyte, CoS_2-C/CNT exhibits excellent rate capability and stable specific capacities of on average 484, 458, 417, 372, 342, 322, and 306 mAh g^{-1} for an applied specific current of 50, 100, 200, 500, 1000, 1500, and 2000 mA g^{-1}, respectively (Figure 8a). After the rate capability test, a specific capacity of 434 mAh g^{-1} was obtained when decreasing the current back to 100 mA g^{-1}, indicating the outstanding reversibility in this electrolyte. Differently, when using the carbonate-based electrolyte, a continuous capacity fading is observed at each current density (see Figure 8b), with only 273 and 110 mAh g^{-1} obtained at 500 and 2000 mA g^{-1}, respectively. Once more, comparing the (dis-)charge profiles of CoS_2-C/CNT anodes in the two different electrolytes (see Figure 8c,d), $NaPF_6$−EC/PC

DOI: 10.1021/acsnano.8b03188
ACS Nano 2018, 12, 7220−7231

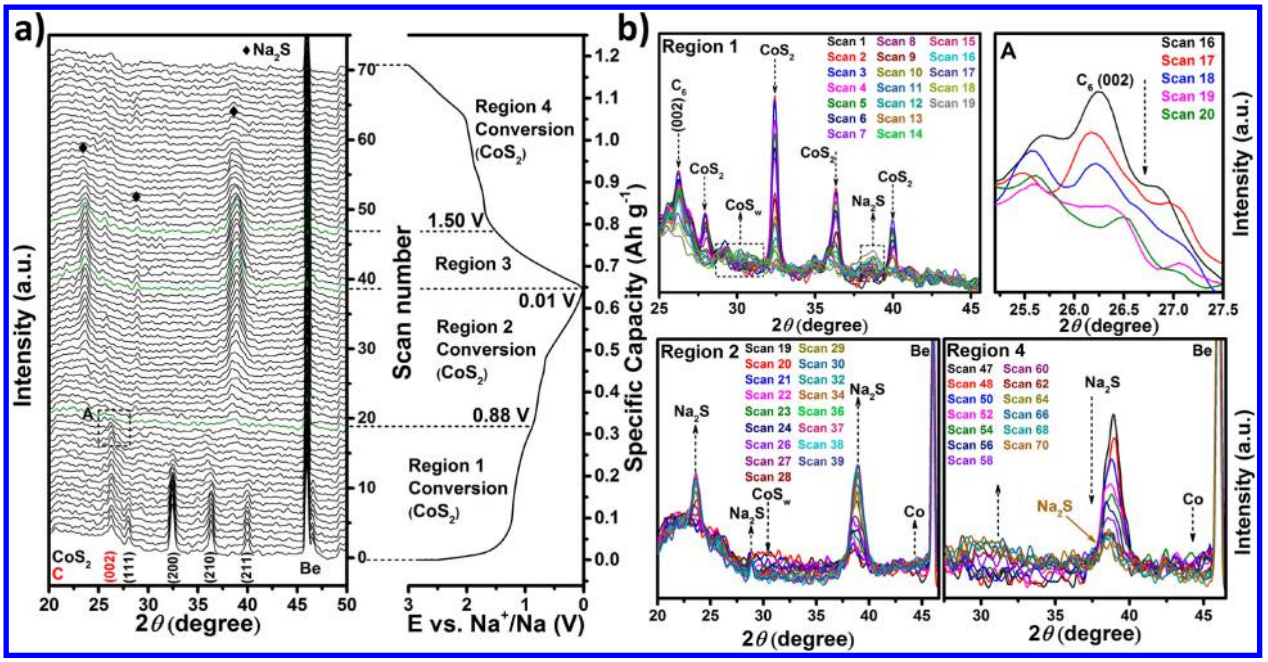

Figure 9. ***In situ*** **XRD analysis of CoS_2-C/CNT-based electrodes galvanostatically (dis-)charged** ***vs*** **sodium metal, using 1 M $NaPF_6$ in DME as electrolyte. (a)** ***In situ*** **recorded XRD patterns (scans 1 to 70; left panel) and the corresponding (dis-)charge profile (right panel). (b) Selected regions of the waterfall plot according to the different occurring electrochemical reactions and distinguished features of the (dis-)charge profile.**

shows a significantly increasing polarization when elevating the applied current, while the DME-based cell reveals a decrease of all (dis-)charge features. According to previous literature results, the rapid capacity fading of the CoS_2-C/CNT electrode in carbonate-based electrolyte is likely attributed to the carbon exfoliation occurring in the PC-based electrolyte.[49−51] However, the improved long-cycling life, rate capability, and reversibility of the CoS_2-C/CNT electrode in 1 M $NaPF_6$−DME electrolyte can be ascribed to (i) the formation of a more stable SEI layer and (ii) the suppressed Na-polysulfide dissolution in DME.[45,50−53] In fact, the Na-ion storage performance reported herein, especially with respect to cycling stability and rate capability, is superior compared to almost all previous studies on CoS_2 or CoS_2-based composites, as summarized in Tables S5 and S6.

In order to potentially explain the difference in achievable capacity compared to the lithium storage mechanism, we conducted an *in situ* XRD analysis of the first discharge and charge for the sodium-based half-cells (Figure 9). The galvanostatic (dis-)charge profile (right part of Figure 9a) can be roughly divided into four different regions (indicated by the olive XRD patterns in Figure 9a, left part). Region 1, from OCV to 0.88 V, covers the evident plateau at around 1.26−1.10 V after the initial almost vertical voltage drop, corresponding to the reduction peak at 1.15 V in the first cathodic sweep of the CV (see Figure 7a). The corresponding XRD patterns (scans 1−19), shown in Figure 9b (region 1), display a rapid intensity decrease of the CoS_2-related reflections until they completely vanish in scan 14/15. Subsequently, a new signal gradually evolves at 38.9° during the scans 15 to 19, suggesting the formation of Na_2S (JCPDS card no. 00-023-0441). Simultaneously, a new, rather broad reflection evolves around 28−32°, indicating the formation of CoS_w (*ca.* 30°). The decreased crystallinity can be presumably attributed to the larger cation radius of Na^+ (Na^+: 1.06 Å *vs* Li^+: 0.76 Å), resulting in the formation of an amorphous phase during the sodiation process.[4,43] Hence, as observed in the case of lithiation, the sodiation of CoS_2 proceeds *via* the intermediate formation of a sulfur-poor CoS_w phase. Furthermore, from scan 15 (1.04 V), the intensity of the (002) signal of graphitic carbon at 26.2° continuously declines until it completely disappears at the end of the voltage plateau at 0.88 V (scan 19). According to previous studies, a decrease in intensity of the (002) reflection indicates the co-intercalation of solvated sodium cations into graphitized carbon. The fact that we do not observe any features indicating a crystalline structure for such a phase might be due to the disordered carbonaceous structure.[43,46]

Upon full discharge to 0.01 V, *i.e.*, in region 2 (from 0.88 to 0.01 V, corresponding to the cathodic peaks at 0.73 and 0.60 V in the CV plots) the XRD patterns (scans 19 to 39) show that the reflections assigned to the sulfur-poor CoS_w phase gradually disappear, while the intensity of the (220) reflection of Na_2S continuously increases, accompanied by the appearance of two new reflections at 23.5° and 27.3°, corresponding to the (111) and (200) planes of Na_2S (JCPDS card no. 00-023-0441), respectively. Meanwhile, a new shoulder of the signal at *ca.* 44.3° is attributed to the formation of metallic Co (JCPDS card no. 15-0806). These data suggest that the sulfur-poor cobalt sulfide phase is further converted to sodium sulfide and metallic cobalt in region 2.

For the following desodiation process, no distinct changes can be observed up to 1.5 V (referred to as region 3, scans 39−47), indicating that the charge storage in this region does not involve any transition of crystalline phases, at least within the detection limits of the instrument used.

Upon further desodiation up to 3.0 V (region 4, corresponding to first anodic peaks at 1.76 and 19.5 V in the CV plots), a rapid intensity decrease of all Na_2S- and Co^0-related features is observed (scans 47−70), while a new, rather broad reflection evolves in the 28−35° range. Notably, the (220) reflection of Na_2S is still observed, even in the last scan (scan 70, 3.0 V). Accordingly, the new reflection may be assigned to the

DOI: 10.1021/acsnano.8b03188
ACS Nano 2018, 12, 7220−7231

formation of a mixture of CoS_2 (at 32.4°) and sulfur-poor CoS_w (at 30°) as result of the partially irreversible conversion.[22,32]

Also interestingly, no carbon-related features are observed anymore in the fully charged state, revealing that it remains highly disordered, *i.e.*, nanocrystalline and/or amorphous.

In conclusion, the first-cycle (de)sodiation mechanism of CoS_2-C/CNT may be summarized as follows, if neglecting the co-intercalation of Na-ether complexes due to the lack of clear evidence about its reversibility for our nanocomposite:

Region 1 (OCV−0.88 V, conversion)

$$CoS_2 + 2Na^+ + 2e^- \rightarrow CoS_w + Na_2S \text{ (not balanced)}$$

Region 2 (0.88−0.01 V, conversion)

$$CoS_w + 2wNa^+ + 2we^- \rightarrow Co^0 + wNa_2S$$

Region 4 (1.5−3.0 V, conversion)

$$2Co^0 + (2 + w)Na_2S \rightarrow CoS_2 + CoS_w + (4 + 2w)Na^+ + (4 + 2w)e^-$$

CONCLUSIONS

A model CoS_2-C/CNT nanocomposite was successfully synthesized by using ZIF-67 as a single precursor. Using a facile two-step synthesis, CoS_2 nanoparticles were uniformly embedded in porous carbonaceous micro-polyhedrons, interwoven by numerous highly conductive CNTs. Importantly, these multiwalled CNTs were directly formed on the surface of micro-polyhedron by a simple pyrolysis of this Co-based ZIF in a N_2 atmosphere. The as-obtained CoS_2-C/CNT nanocomposite possesses several appealing features such as moderate surface area, suitable pore size distribution, interior void, and numerous active sites, resulting in fast mass transport and excellent strain accommodation. Benefiting from these advantages, the resulting CoS_2-C/CNT composite displays outstanding lithium and sodium storage properties. Specifically, when evaluated as active material in LIBs, the composite electrode showed a high reversible capacity of 1030 mAh g^{-1} at 0.1 A g^{-1} (after 120 cycles) and 510 mAh g^{-1} at 1.0 A g^{-1} (after 500 cycles) as well as good rate performance with 433 mAh g^{-1} at 2.5 A g^{-1}. Quantitative kinetic analysis, however, demonstrates that the fast Li-ion storage and the impressive rate performance mostly derive from pseudocapacitive contribution.

For sodium-ion storage, the long-cycling performance and rate capability were significantly improved by utilizing ether-based (DME) instead of carbonate-based electrolyte. A large reversible capacity of 403 mAh g^{-1} at 0.1 A g^{-1} (after 200 cycles) was obtained with excellent cycling stability (capacity retention up to 90% after 200 cycles) and outstanding CE (initial CE of 82% and cyclic CE of ~99.9%), accompanied by an excellent rate performance (306 mAh g^{-1} at 2.0 A g^{-1}). More importantly, the structural variation taking place in the CoS_2-C/CNT nanocomposite during the initial (de)lithiation and (de)-sodiation has been studied by *in situ* XRD. The results reveal a two-step conversion reaction mechanism of CoS_2 to form metallic Co and Li_2S/Na_2S.

While cobalt sulfide will presumably not play a decisive role for commercial battery applications—due to the limited availability of cobalt—the herein presented results may serve as a model study for other transition metal sulfides and, thus, foster the research on (transition) metal sulfides as active material for secondary batteries in general.

METHODS

Synthesis of ZIF-67. Cobalt(II) nitrate hexahydrate ($Co(NO_3)_2 \cdot 6H_2O$, 98%) and 2-methylimidazole (2-MeIm, 99%) were obtained from Sigma-Aldrich. Methanol (dried, 0.003% H_2O) was purchased from SeccoSolv. Typically, to prepare the ZIF-67 precursor, $Co(NO_3)_2 \cdot 6H_2O$ (30 mmol, 8.732 g) was first dissolved in 0.3 L of methanol. Then, the solution was added to a solution of 2-MeIm (120 mmol, 9.84 g) in 0.1 L of methanol. After vigorous stirring at room temperature for 30 min, the mixed solution was aged at *ca.* 20−25 °C for 48 h. The as-obtained purple precipitate was collected, washed five times with methanol *via* centrifugation, and dried at 60 °C overnight.

Synthesis of Co-C/CNT and CoS_2-C/CNT. For obtaining the compound labeled as Co-C/CNT, the purple ZIF-67 precursor powder (700 mg) was carbonized at 900 °C for 10 h in a tube furnace under N_2 (heating ramp: 5 °C min^{-1}). After cooling, the sample color changed from purple (ZIF-67) to black (Co-C/CNT). The black Co-C/CNT powder was then mixed with sulfur (mass ratio of 1:2.5) in a mortar, and the mixture was placed in a tube furnace and then heated to 300 °C (heating ramp: 10 °C min^{-1}) for 2 h under N_2. Finally, the furnace was cooled to room temperature, and the CoS_2-C/CNT black powder was recovered.

Materials Characterization. The morphological features of the ZIF-67 and Co-C/CNT precursors as well as the CoS_2-C/CNT nanocomposite were investigated *via* SEM and TEM carried out on a ZEISS 1550VP and a JEOL JEM-3000, respectively. Meanwhile, information about the chemical composition of CoS_2-C/CNT was obtained by elemental mapping using EDX. The lattice fringes of Co-C/CNT and CoS_2-C/CNT were studied by an imaging Cs-corrected HRTEM, applying an acceleration voltage in the range of 80 to 300 kV (FEI Titan 80-300 kV transmission electron microscope). Powder XRD (Bruker D8 Advance; Cu Kα radiation; λ = 0.154 nm) was employed to determine the crystal structure of Co-C/CNT and CoS_2-C/CNT. The BET specific surface area of the samples was derived from the nitrogen absorption−desorption isotherms (Autosorb-iQ, Quantachrome) at 77 K. Raman spectra of CoS_2-C/CNT were collected using a confocal InVia Raman microspectrometer (from Renishaw), equipped with a 633 nm laser. TGA (TA Instruments, model Q5000) was performed to determine the content of CoS_2 in CoS_2-C/CNT. The tests were performed under an air flow with a heating rate of 2 °C min^{-1}. Finally, the Co content of the CoS_2-C/CNT was determined by ICP-OES. For this, the as-obtained CoS_2-C/CNT sample was dissolved in hot hydrochloric acid and investigated by means of a Spectro Arcos (Spectro Analytical Instruments) with axial plasma view. XPS measurements were conducted on a PHI 5800 MultiTechnique ESCA system with monochromatized Al Kα (1486.6 eV) radiation at a takeoff angle of 45°. The electronic conductivity of CoS_2-C/CNT has been examined by using a torque cell in the frequency range from 1 to 10^6 Hz at room temperature (298 K).

Electrochemical Measurements. The working electrodes were composed of 80 wt % CoS_2-C/CNT or Co-C/CNT as active material, 10 wt % SuperC65 (TIMCAL) as conductive carbon, and 10 wt % polyvinylidene fluoride (PVdF) as binder. For the preparation, PVdF was first dissolved in *N*-methylpyrrolidinone (Sigma-Aldrich) to obtain a 5 wt % solution. Subsequently, the active material and the conductive carbon were added, and the suspension was mixed by magnetic stirring overnight. The resulting slurry was cast on dendritic copper foil (Schlenk, 99.9%) by means of a laboratory doctor blade with a wet film thickness of 120 μm. After drying in an oven at 60 °C overnight, disk electrodes (12 mm in diameter) were punched and vacuum-dried for 24 h at 120 °C. The average active material mass loading was in the range of *ca.* 1.5−1.7 mg cm^{-2}. The electrochemical tests for the characterization as lithium-ion electrode were performed in stainless steel 2032 coin cells with lithium metal foil (Rockwood Lithium, battery grade) serving as reference and counter electrode and a sheet of glass fiber (GF/D, Whatman) serving as separator. The electrolyte (UBE) was a 1 M solution of $LiPF_6$ in a 1:1 (volume) mixture of EC and diethyl carbonate (DEC), including 1% (volume) vinylene carbonate (VC). For the SIB tests, three-electrode Swagelok-type cells with Na metal as reference and counter electrode were employed instead. As electrolyte a

DOI: 10.1021/acsnano.8b03188
ACS Nano 2018, 12, 7220−7231

1 M solution of $NaPF_6$ in DME or EC/PC (1:1 by weight) was employed. The coin cells and Swagelok-type cells were assembled in a glovebox (MBraun UNIlab; H_2O and O_2 content <0.1 ppm). The potential and voltage values given herein refer to the Li/Li^+ or Na/Na^+ quasi-reference couple, depending on the targeted battery application. All electrochemical tests were performed at 20 ± 2 °C. Galvanostatic cycling was conducted using a Maccor 3000 battery tester, fixing the potential range to 0.01−3.0 V (*vs* Li/Li^+ or Na/Na^+). CV was performed utilizing a VMP3 potentiostat (Biologic Science Instruments) in the same voltage range, *i.e.*, 0.01−3.0 V *vs* Li/Li^+ or Na/Na^+.

***In Situ* XRD Measurements.** The *in situ* XRD experiments with CoS_2-C/CNT as active material for LIBs and SIBs were performed in a self-designed two-electrode cell.[22,25,54] The working electrode was composed of 75 wt % CoS_2-C/CNT, 15 wt % SuperC65, and 15 wt % PVdF, cast directly on the beryllium (Be) disk, serving simultaneously as current collector and "window" for the X-ray beam. The wet film thickness was set to 250 μm. The coated Be disks were first dried at 60 °C for 1 h and then at 50 °C under vacuum overnight. Lithium or sodium metal foils were used as counter and reference electrode. A bilayer of Whatman glass fiber (GF/D) served as separator, which was soaked with 400 μL of 1 M $LiPF_6$ in EC/DEC (1:1 volume) added with 1% VC (LIBs) or 1 M $NaPF_6$ in DME (SIBs). One XRD pattern accounted for 1883.6 s (about 30 min). Simultaneously, the cell was galvanostatically (dis-)charged using a potentiostat/galvanostat (SP-150, BioLogic) and applying a specific current of 58 mA g^{-1} (LIBs) or 30 mA g^{-1} (SIBs) within a potential range of 0.01−3.0 V.

ASSOCIATED CONTENT

Supporting Information

The Supporting Information is available free of charge on the ACS Publications website at DOI: 10.1021/acsnano.8b03188.

XRD pattern of the Co-C/CNT; particle size distribution of metallic Co and CoS_2; XPS, EDX, TGA, ICP, Raman spectrum, and BET/BJH of the CoS_2-C/CNT; electrochemical data of the CoS_2-C/CNT includes CV curves at different sweep rates and *ex situ* SEM/TEM images; LIBs' long-term cycling performance of Co-C/CNT-based electrodes (PDF)

AUTHOR INFORMATION

Corresponding Authors

*E-mail: alberto.varzi@kit.edu (A. Varzi).
*E-mail: stefano.passerini@kit.edu (S. Passerini).

ORCID

Dominic Bresser: 0000-0001-6429-6048
Carsten Streb: 0000-0002-5846-1905
Alberto Varzi: 0000-0001-5069-0589
Stefano Passerini: 0000-0002-6606-5304

Notes

The authors declare no competing financial interest.

ACKNOWLEDGMENTS

The authors thank Dr. Kim, Xinwei Dou, Huang Zhang, and Bingsheng Qin for the valuable discussions. Y.M. and Y.-J.M. gratefully acknowledge financial support from the Chinese Scholarship Council (CSC, No. 201608080085; No. 201608080094). Financial support from the Helmholtz Association and Ulm University is acknowledged. Furthermore, the authors would like to thank Dr. Diemant for XPS testing and Hosseini for electronic conductivity testing.

REFERENCES

(1) Bresser, D.; Passerini, S.; Scrosati, B. Leveraging Valuable Synergies by Combining Alloying and Conversion for Lithium-Ion Anodes. *Energy Environ. Sci.* **2016**, *9*, 3348−3367.
(2) Scrosati, B.; Garche, J. Lithium Batteries: Status, Prospects and Future. *J. Power Sources* **2010**, *195*, 2419−2430.
(3) Tarascon, J.-M.; Armand, M. Issues and Challenges Facing Rechargeable Lithium Batteries. *Nature* **2001**, *414*, 359−367.
(4) Hasa, I.; Hassoun, J.; Passerini, S. Nanostructured Na-Ion and Li-Ion Anodes for Battery Application: A Comparative Overview. *Nano Res.* **2017**, *10*, 3942−3969.
(5) Lin, Y.; Qiu, Z.; Li, D.; Ullah, S.; Hai, Y.; Xin, H.; Liao, W.; Yang, B.; Fan, H.; Xu, J.; Zhu, C. NiS_2@CoS_2 Nanocrystals Encapsulated in N-Doped Carbon Nanocubes for High Performance Lithium/Sodium Ion Batteries. *Energy Storage Mater.* **2018**, *11*, 67−74.
(6) Wang, X.; Liu, X.; Wang, G.; Xia, Y.; Wang, H. One-Dimensional Hybrid Nanocomposite of High-Density Monodispersed Fe_3O_4 Nanoparticles and Carbon Nanotubes for High-Capacity Storage of Lithium and Sodium. *J. Mater. Chem. A* **2016**, *4*, 18532−18542.
(7) Wang, X.; Chen, K.; Wang, G.; Liu, X.; Wang, H. Rational Design of Three-Dimensional Graphene Encapsulated with Hollow FeP@Carbon Nanocomposite as Outstanding Anode Material for Lithium Ion and Sodium Ion Batteries. *ACS Nano* **2017**, *11*, 11602−11616.
(8) Mei, P.; Pramanik, M.; Lee, J.; Ide, Y.; Alothman, Z. A.; Kim, J. H.; Yamauchi, Y. Highly Ordered Mesostructured Vanadium Phosphonate toward Electrode Materials for Lithium-Ion Batteries. *Chem. - Eur. J.* **2017**, *23*, 4344−4352.
(9) Xiao, Y.; Hwang, J.-Y.; Belharouak, I.; Sun, Y.-K. Superior Li/Na-Storage Capability of a Carbon-Free Hierarchical CoS_x Hollow Nanostructure. *Nano Energy* **2017**, *32*, 320−328.
(10) Wang, Q.; Zou, R.; Xia, W.; Ma, J.; Qiu, B.; Mahmood, A.; Zhao, R.; Yang, Y.; Xia, D.; Xu, Q. Facile Synthesis of Ultrasmall CoS_2 Nanoparticles within Thin N-Doped Porous Carbon Shell for High Performance Lithium-Ion Batteries. *Small* **2015**, *11*, 2511−2517.
(11) Zhang, Y.; Wang, N.; Sun, C.; Lu, Z.; Xue, P.; Tang, B.; Bai, Z.; Dou, S. 3D Spongy CoS_2 Nanoparticles/Carbon Composite as High-Performance Anode Material for Lithium/Sodium Ion Batteries. *Chem. Eng. J.* **2018**, *332*, 370−376.
(12) Zhang, J.; Yu, L.; Lou, X. W. D. Embedding CoS_2 Nanoparticles in N-Doped Carbon Nanotube Hollow Frameworks for Enhanced Lithium Storage Properties. *Nano Res.* **2017**, *10*, 4298−4304.
(13) Furukawa, H.; Cordova, K. E.; O'Keeffe, M.; Yaghi, O. M. The Chemistry and Applications of Metal-Organic Frameworks. *Science* **2013**, *341*, 1230444.
(14) Xia, W.; Mahmood, A.; Zou, R.; Xu, Q. Metal−Organic Frameworks and Their Derived Nanostructures for Electrochemical Energy Storage and Conversion. *Energy Environ. Sci.* **2015**, *8*, 1837−1866.
(15) Ma, Y.; Ma, H.; Yang, Z.; Ma, J.; Su, Y.; Li, W.; Lei, Z. Methyl Cinnamate-Derived Fluorescent Rigid Organogels Based on Cooperative $\pi-\pi$ Stacking and C═O···π Interactions Instead of H-Bonding and Alkyl Chains. *Langmuir* **2015**, *31*, 4916−4923.
(16) Su, P.; Xiao, H.; Zhao, J.; Yao, Y.; Shao, Z.; Li, C.; Yang, Q. Nitrogen-Doped Carbon Nanotubes Derived from Zn−Fe-ZIF Nanospheres and Their Application as Efficient Oxygen Reduction Electrocatalysts with *in Situ* Generated Iron Species. *Chem. Sci.* **2013**, *4*, 2941−2946.
(17) Han, F.; Lv, T.; Sun, B.; Tang, W.; Zhang, C.; Li, X. *In Situ* Formation of Ultrafine CoS_2 Nanoparticles Uniformly Encapsulated in N/S-Doped Carbon Polyhedron for Advanced Sodium-Ion Batteries. *RSC Adv.* **2017**, *7*, 30699−30706.
(18) Li, Y.; Jia, B.; Fan, Y.; Zhu, K.; Li, G.; Su, C.-Y. Bimetallic Zeolitic Imidazolite Framework Derived Carbon Nanotubes Embedded with Co Nanoparticles for Efficient Bifunctional Oxygen Electrocatalyst. *Adv. Energy Mater.* **2018**, *8*, 1702048.
(19) Gadipelli, S.; Zhao, T.; Shevlin, S. A.; Guo, Z. Switching Effective Oxygen Reduction and Evolution Performance by Controlled Graphitization of a Cobalt−Nitrogen−Carbon Framework System. *Energy Environ. Sci.* **2016**, *9*, 1661−1667.

DOI: 10.1021/acsnano.8b03188
ACS Nano 2018, 12, 7220−7231

(20) Xia, B. Y.; Yan, Y.; Li, N.; Wu, H. B.; Lou, X. W. D.; Wang, X. A Metal−Organic Framework-Derived Bifunctional Oxygen Electrocatalyst. *Nat. Energy* **2016**, *1*, 15006.
(21) Wu, R.; Wang, D. P.; Rui, X.; Liu, B.; Zhou, K.; Law, A. W. K.; Yan, Q.; Wei, J.; Chen, Z. *In-Situ* Formation of Hollow Hybrids Composed of Cobalt Sulfides Embedded within Porous Carbon Polyhedra/Carbon Nanotubes for High-Performance Lithium-Ion Batteries. *Adv. Mater.* **2015**, *27*, 3038−3044.
(22) Ma, Y.; Ma, Y.; Geiger, D.; Kaiser, U.; Zhang, H.; Kim, G.-T.; Diemant, T.; Behm, R. J.; Varzi, A.; Passerini, S. ZnO/$ZnFe_2O_4$/N-Doped C Micro-Polyhedrons with Hierarchical Hollow Structure as High-Performance Anodes for Lithium-Ion Batteries. *Nano Energy* **2017**, *42*, 341−352.
(23) Zhu, L.; Susac, D.; Teo, M.; Wong, K.; Wong, P.; Parsons, R.; Bizzotto, D.; Mitchell, K.; Campbell, S. Investigation of CoS_2-Based Thin Films as Model Catalysts for the Oxygen Reduction Reaction. *J. Catal.* **2008**, *258*, 235−242.
(24) Iwasaki, T.; Zelai, T.; Ye, S.; Tsuchiya, Y.; Chong, H. M. H.; Mizuta, H. Local Hole Doping Concentration Modulation on Graphene Probed by Tip-Enhanced Raman Spectroscopy. *Carbon* **2017**, *111*, 67−73.
(25) Bresser, D.; Paillard, E.; Kloepsch, R.; Krueger, S.; Fiedler, M.; Schmitz, R.; Baither, D.; Winter, M.; Passerini, S. Carbon Coated $ZnFe_2O_4$ Nanoparticles for Advanced Lithium-Ion Anodes. *Adv. Energy Mater.* **2013**, *3*, 513−523.
(26) Ma, Y.; Wang, H.; Feng, H.; Ji, S.; Mao, X.; Wang, R. Three-Dimensional Iron, Nitrogen-Doped Carbon Foams as Efficient Electrocatalysts for Oxygen Reduction Reaction in Alkaline Solution. *Electrochim. Acta* **2014**, *142*, 317−323.
(27) Yang, S. J.; Nam, S.; Kim, T.; Im, J. H.; Jung, H.; Kang, J. H.; Wi, S.; Park, B.; Park, C. R. Preparation and Exceptional Lithium Anodic Performance of Porous Carbon-Coated ZnO Quantum Dots Derived from a Metal−Organic Framework. *J. Am. Chem. Soc.* **2013**, *135*, 7394−7397.
(28) Ma, Y.; Wang, H.; Ji, S.; Goh, J.; Feng, H.; Wang, R. Highly Active Vulcan Carbon Composite for Oxygen Reduction Reaction in Alkaline Medium. *Electrochim. Acta* **2014**, *133*, 391−398.
(29) Huang, G.; Zhang, F.; Du, X.; Qin, Y.; Yin, D.; Wang, L. Metal Organic Frameworks Route to *in Situ* Insertion of Multiwalled Carbon Nanotubes in Co_3O_4 Polyhedra as Anode Materials for Lithium-Ion Batteries. *ACS Nano* **2015**, *9*, 1592−1599.
(30) Su, Q.; Xie, J.; Zhang, J.; Zhong, Y.; Du, G.; Xu, B. *In Situ* Transmission Electron Microscopy Observation of Electrochemical Behavior of CoS_2 in Lithium-Ion Battery. *ACS Appl. Mater. Interfaces* **2014**, *6*, 3016−3022.
(31) Kong, S.; Jin, Z.; Liu, H.; Wang, Y. Morphological Effect of Graphene Nanosheets on Ultrathin CoS Nanosheets and Their Applications for High-Performance Li-Ion Batteries and Photocatalysis. *J. Phys. Chem. C* **2014**, *118*, 25355−25364.
(32) Mueller, F.; Geiger, D.; Kaiser, U.; Passerini, S.; Bresser, D. Elucidating the Impact of Cobalt Doping on the Lithium Storage Mechanism in Conversion/Alloying-Type Zinc Oxide Anodes. *ChemElectroChem* **2016**, *3*, 1311−1319.
(33) Aurbach, D.; Ein-Eli, Y. The Study of Li-Graphite Intercalation Processes in Several Electrolyte Systems Using *in Situ* X-Ray Diffraction. *J. Electrochem. Soc.* **1995**, *142*, 1746−1752.
(34) Bresser, D.; Mueller, F.; Fiedler, M.; Krueger, S.; Kloepsch, R.; Baither, D.; Winter, M.; Paillard, E.; Passerini, S. Transition-Metal-Doped Zinc Oxide Nanoparticles as a New Lithium-Ion Anode Material. *Chem. Mater.* **2013**, *25*, 4977−4985.
(35) Ma, Y.; Ulissi, U.; Bresser, D.; Ma, Y.; Ji, Y.; Passerini, S. Manganese Silicate Hollow Spheres Enclosed in Reduced Graphene Oxide as Anode for Lithium-Ion Batteries. *Electrochim. Acta* **2017**, *258*, 535−543.
(36) Ponrouch, A.; Taberna, P.-L.; Simon, P.; Palacín, M. R. On the Origin of the Extra Capacity at Low Potential in Materials for Li Batteries Reacting through Conversion Reaction. *Electrochim. Acta* **2012**, *61*, 13−18.
(37) Sun, H.; Xin, G.; Hu, T.; Yu, M.; Shao, D.; Sun, X.; Lian, J. High-Rate Lithiation-Induced Reactivation of Mesoporous Hollow Spheres for Long-Lived Lithium-Ion Batteries. *Nat. Commun.* **2014**, *5*, 4526.
(38) Chao, D.; Liang, P.; Chen, Z.; Bai, L.; Shen, H.; Liu, X.; Xia, X.; Zhao, Y.; Savilov, S. V.; Lin, J.; Shen, Z. X. Pseudocapacitive Na-Ion Storage Boosts High Rate and Areal Capacity of Self-Branched 2D Layered Metal Chalcogenide Nanoarrays. *ACS Nano* **2016**, *10*, 10211−10219.
(39) Augustyn, V.; Come, J.; Lowe, M. A.; Kim, J. W.; Taberna, P.-L.; Tolbert, S. H.; Abruña, H. D.; Simon, P.; Dunn, B. High-Rate Electrochemical Energy Storage through Li^+ Intercalation Pseudocapacitance. *Nat. Mater.* **2013**, *12*, 518−522.
(40) Muller, G. A.; Cook, J. B.; Kim, H.-S.; Tolbert, S. H.; Dunn, B. High Performance Pseudocapacitor Based on 2D Layered Metal Chalcogenide Nanocrystals. *Nano Lett.* **2015**, *15*, 1911−1917.
(41) Hu, X.; Li, C.; Lou, X.; Yang, Q.; Hu, B. Hierarchical CuO Octahedra Inherited from Copper Metal−Organic Frameworks: High-Rate and High-Capacity Lithium-Ion Storage Materials Stimulated by Pseudocapacitance. *J. Mater. Chem. A* **2017**, *5*, 12828−12837.
(42) Yan, J. M.; Huang, H. Z.; Zhang, J.; Liu, Z. J.; Yang, Y. A Study of Novel Anode Material CoS_2 for Lithium Ion Battery. *J. Power Sources* **2005**, *146*, 264−269.
(43) Wen, Y.; He, K.; Zhu, Y.; Han, F.; Xu, Y.; Matsuda, I.; Ishii, Y.; Cumings, J.; Wang, C. Expanded Graphite as Superior Anode for Sodium-Ion Batteries. *Nat. Commun.* **2014**, *5*, 4033.
(44) Zhu, X.; Meng, Z.; Ying, H.; Xu, X.; Xu, F.; Han, W. A Novel CoS_2/Reduced Graphene Oxide/Multiwall Carbon Nanotubes Composite as Cathode for High Performance Lithium Ion Battery. *Chem. Phys. Lett.* **2017**, *684*, 191−196.
(45) Shadike, Z.; Cao, M.-H.; Ding, F.; Sang, L.; Fu, Z.-W. Improved Electrochemical Performance of CoS_2−MWCNT Nanocomposites for Sodium-Ion Batteries. *Chem. Commun.* **2015**, *51*, 10486−10489.
(46) Kim, H.; Hong, J.; Yoon, G.; Kim, H.; Park, K.-Y.; Park, M.-S.; Yoon, W.-S.; Kang, K. Sodium Intercalation Chemistry in Graphite. *Energy Environ. Sci.* **2015**, *8*, 2963−2969.
(47) Kim, H.; Hong, J.; Park, Y.-U.; Kim, J.; Hwang, I.; Kang, K. Sodium Storage Behavior in Natural Graphite Using Ether-Based Electrolyte Systems. *Adv. Funct. Mater.* **2015**, *25*, 534−541.
(48) Wu, L.; Bresser, D.; Buchholz, D.; Passerini, S. Nanocrystalline TiO_2(B) as Anode Material for Sodium-Ion Batteries. *J. Electrochem. Soc.* **2015**, *162*, A3052−A3058.
(49) Cabello, M.; Bai, X.; Chyrka, T.; Ortiz, G. F.; Lavela, P.; Alcántara, R.; Tirado, J. L. On the Reliability of Sodium Co-Intercalation in Expanded Graphite Prepared by Different Methods as Anodes for Sodium-Ion Batteries. *J. Electrochem. Soc.* **2017**, *164*, A3804−A3813.
(50) Shi, P. C.; Lin, M.; Zheng, H.; He, X. D.; Xue, Z. M.; Xiang, H. F.; Chen, C. H. Effect of Propylene Carbonate-Li^+ Solvation Structures on Graphite Exfoliation and Its Application in Li-Ion Batteries. *Electrochim. Acta* **2017**, *247*, 12−18.
(51) Hu, Z.; Zhu, Z.; Cheng, F.; Zhang, K.; Wang, J.; Chen, C.; Chen, J. Pyrite FeS_2 for High-Rate and Long-Life Rechargeable Sodium Batteries. *Energy Environ. Sci.* **2015**, *8*, 1309−1316.
(52) Fan, X.; Gao, T.; Luo, C.; Wang, F.; Hu, J.; Wang, C. Superior Reversible Tin Phosphide-Carbon Spheres for Sodium Ion Battery Anode. *Nano Energy* **2017**, *38*, 350−357.
(53) Zhu, Y.; Suo, L.; Gao, T.; Fan, X.; Han, F.; Wang, C. Ether-Based Electrolyte Enabled Na/FeS_2 Rechargeable Batteries. *Electrochem. Commun.* **2015**, *54*, 18−22.
(54) Varzi, A.; Mattarozzi, L.; Cattarin, S.; Guerriero, P.; Passerini, S. 3D Porous Cu-Zn Alloys as Alternative Anode Materials for Li-Ion Batteries with Superior Low *T* Performance. *Adv. Energy Mater.* **2018**, *8*, 1701706.

DOI: 10.1021/acsnano.8b03188
ACS Nano 2018, 12, 7220−7231